Materials Advances

ROYAL SOCIETY OF CHEMISTRY

PAPER

View Article Online
View Journal

Cite this: DOI: 10.1039/d6ma00291a

A novel zirconium-based metal organic framework with record adsorption of PFOA in aqueous solution

Xiaoyun Su,[a] Bo Yuan,[a] Peng Luo,[a] Wei Xu,*[a] Wen-Cai Ye *[ab] and Ren-Wang Jiang *[ab]

Received 3rd March 2026,
Accepted 10th June 2026

DOI: 10.1039/d6ma00291a

rsc.li/materials-advances

Perfluorooctanoic acid (PFOA), an emerging contaminant of growing concern in recent years, is widely distributed in aquatic environments. Characterized by its robust chemical structure and persistence against natural degradation, PFOA poses significant threats to human health due to its bioaccumulation and carcinogenicity. Therefore, there is an urgent need to develop efficient methods for its removal from aqueous solutions. In this work, we report a novel, highly stable zirconium-based metal–organic framework (Zr-705) featuring hexagonal cavities with a pore size of 2.5 nm. The cavity is functionalized with additional phenyl groups that provide additional adsorption sites. Remarkably, Zr-705 exhibits outstanding PFOA adsorption performance, including a record adsorption capacity (2031 mg g^{-1}), rapid uptake rate (2.25 mg mg^{-1} h^{-1}), and excellent selectivity and reusability. Furthermore, we developed a novel PFOA capture device based on a Zr-705 packed column, which demonstrates outstanding PFOA removal efficiency and water purification performance.

Introduction

PFOA, a highly persistent pollutant, consists of a hydrophobic perfluorinated alkyl chain and a hydrophilic carboxylic acid group.[1] All hydrogen atoms on the alkyl chain are replaced by fluorine atoms. Due to the high strength of the carbon–fluorine bond (488 kJ mol^{-1}) and the simultaneous hydrophobicity and hydrophilicity, PFOA is commonly used as a highly effective surfactant and surface protectant.[2] These properties have led to its widespread use in diverse applications, including the photographic and semiconductor industries, coatings and paints, firefighting foams, medical devices, personal care products and printing.[3] PFOA is ubiquitously detected in soil, and underground and surface waterbodies.[4–6] In particular, near fluoropolymer manufacturing sites, PFOA concentrations can reach levels as high as 0.97 mg L^{-1}. The widespread use of PFOA, coupled with its persistence as an environmental contaminant, has raised significant scientific and public health concerns.[4,7,8] PFOA was listed on the U.S. Environmental Protection Agency's (EPA) Contaminant Candidate List in 2021 and classified as a "likely human carcinogen".[4] Furthermore, it was added to the List of Key New Pollutants for Priority Control by China's Ministry of Ecology and Environment in 2023.[9]

Notably, drinking water is the primary exposure route for human intake of PFOA.[10] PFOA has been detected in many human specimens such as breast milk, maternal serum, cord blood and blood serum.[11] PFOA exerts multi-system toxic effects in humans, impacting key physiological systems including bone,[12] immune,[13,14] endocrine,[15,16] renal,[17,18] reproductive[19] and hepatic functions.[20,21] PFOA demonstrates notable accumulation in renal tissue, and the active renal reabsorption mechanisms significantly prolong the biological half-life.[22] As the primary target, the liver exhibits persistent histopathological alterations following PFOA exposure.[23] PFOA exposure has also been associated with adverse health outcomes including thyroid dysfunction,[24] embryotoxicity[25] and reduced infant birth weight.[26]

Due to the widespread distribution of PFOA and its resistance to natural degradation and metabolism, it poses various threats to human health, making the need to remove PFOA from the environment urgent. In previous studies, various technologies have been developed to address the PFAS crisis, including bioremediation,[27–29] electrocoagulation,[30,31] foam fractionation,[32,33] sonolysis,[34,35] mechanochemistry,[36,37] electrochemical degradation,[38,39] electron beam[40] and plasma treatment.[41,42] These methods are energy-intensive, time-consuming,

[a] State Key Laboratory of Bioactive Molecules and Druggability Assessment, Guangdong Basic Research Center of Excellence for Natural Bioactive Molecules and Discovery of Innovative Drugs, College of Pharmacy, Jinan University, Guangzhou, China. E-mail: trwjiang@jnu.edu.cn, chywc@aliyun.com, xwnail2003@163.com

[b] International Cooperative Laboratory of Traditional Chinese Medicine Modernization and Innovative Drug Development of Ministry of Education (MOE) of China, Jinan University, Guangzhou, China

and require specific operational conditions, which collectively hinder their large-scale implementation.[43] Considering practical operational challenges and removal efficiency, adsorption has become a common method for PFOA remediation. For example, granular activated carbon (GAC) is widely used to capture PFOA from waterbodies. However, this approach is limited by long treatment time and low efficiency.[1]

Metal–organic frameworks (MOFs), constructed from metal clusters as connecting nodes and organic ligands as linkers, are infinite and periodic network structures containing cavities or channels. MOFs have been used for PFOA treatment, *e.g.* MIL-125-NH_2[44] and MIL-177-HT[45] were used for the photocatalytic degradation of PFOA. PCN-1003, a nickel-based MOF, also demonstrated a high adsorption capacity towards PFOA.[46] Among the reported MOFs, a zirconium-based metal–organic framework (Zr-MOF), featuring zirconium-oxo clusters as the metal nodes, could form highly stable zirconium-oxygen bonds with the carboxylate or sulfonic anions of PFAS. Besides the outstanding performance of Zr-MOFs in diverse fields, including sensing,[47,48] catalysis,[49,50] drug delivery,[51,52] and enzyme immobilization[53–55] and the crystal sponge properties,[56] they showed significant potential for PFOA adsorption due to their high stability and tunable cavities. Several Zr-MOFs, such as NU-1000,[57] PCN-999,[58] UIO-66,[59] PCN-1001[60] and PCN-1002,[60] have been reported for PFOA capture. Therefore, it is feasible to design new Zr-MOFs with high adsorption capacities to further improve the PFOA adsorption efficiency and advance their practical implementation.

In this work, we designed and synthesized a novel zirconium-based metal–organic framework, designated as Zr-705. This framework was constructed by coordination of an anthracene-core tetracarboxylic acid ligand with zirconium clusters in a (4,8)-connected fashion, yielding a csq topological network. The structure features one-dimensional mesoporous channels along the *c*-axis with a pore aperture of 2.5 nm. Notably, one phenyl ring of the anthracene moiety was oriented toward the channel interior, providing enhanced surface area and additional binding sites. Zr-705 exhibited exceptional PFOA adsorption performance, achieving a maximum capacity of 2031 mg g^{-1}. The material also demonstrated rapid adsorption kinetics, facile reusability, and strong anti-interference capability against co-existing impurities.

Results and discussion

Synthesis and characterization

Zr-705 was synthesized by a solvothermal reaction using 5′,5′′′′-(anthracene-9,10-diyl)bis(([1,1′:3′,1″-terphenyl]-4,4″-dicarboxylic acid)) as the ligand (**L1**), zirconium tetrachloride ($ZrCl_4$) as the metal source, *N*,*N*-diethylformamide (DEF) as the solvent, and benzoic acid (BA) and trifluoroacetic acid (TFA) as the modulators. The reaction directly yielded colorless rod-shaped single crystals suitable for structural analysis (Fig. 1). We repeated the synthesis three times under the same conditions, and found that the process was reproducible. Single-crystal X-ray

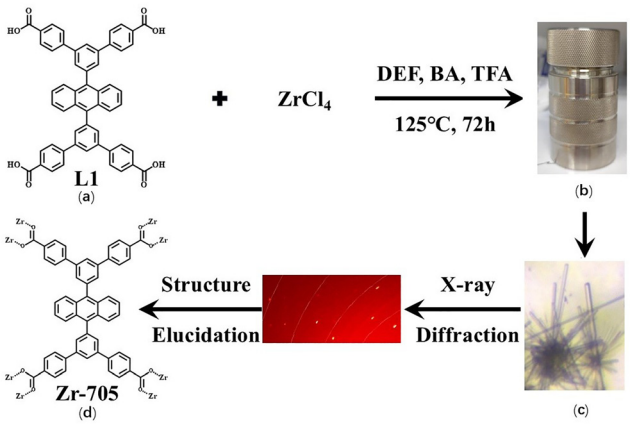

Fig. 1 Synthesis and structural analysis of Zr-705. (a) Ligand structure; (b) solvothermal reaction in a Teflon-lined steel autoclave; (c) crystal images (70–160 μm, visible to the naked eye); (d) structure of Zr-705.

diffraction (SC-XRD) analysis reveals that Zr-705 crystallizes in the hexagonal *P6/mmm* space group with lattice parameters a = 39.9642(12) Å, b = 39.9642(12) Å, c = 20.3746(5) Å, $\alpha = \beta = 90^\circ$, $\gamma = 120^\circ$. The framework consists of a classic Zr_6O_8 cluster core and tetracarboxylate ligands. Each metal node comprises six zirconium atoms bridged by eight μ_3-O groups, forming an octahedral configuration with D_{4h} symmetry (Fig. 2a). Of the 12 edges in the metal octahedral cluster, 8 edges are connected to ligand **L1** through coordination between carboxylate groups and the metal centers (Fig. 2b). The remaining zirconium coordination sites are occupied by eight terminal water molecules, resulting in the final cluster formulation of $Zr_6(\mu_3\text{-}O)_8(H_2O)_8(COO)_8$. Topologically, the **L1** ligand serves as a 4-connected node, while the Zr_6 cluster acts as an 8-connected node, forming a (4,8)-connected csq topology. PLATON calculations[61,62] reveal a total solvent-accessible volume of 22 653.2 $Å^3$, which accounts for

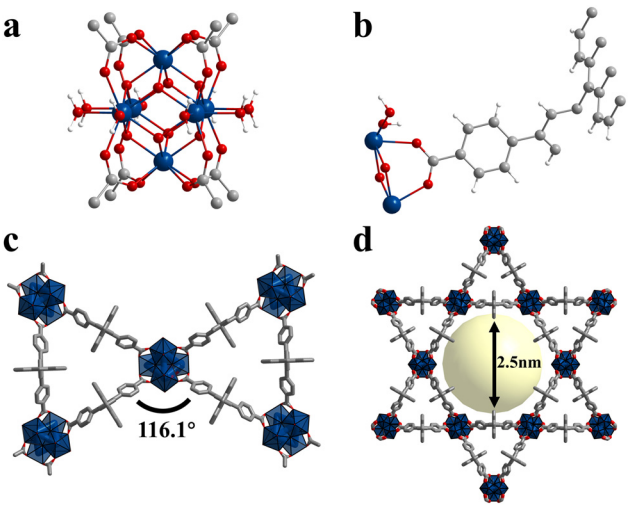

Fig. 2 Zr-MOF 705 structure. (a) Zr metal cluster. (b) The asymmetric unit. (c) The angle of the cavity (H atoms omitted). (d) Cavity size in Zr-705 (viewed along the *c*-axis, H atoms omitted). (Zr: blue, O: red, C: gray, H: white).

80.4% of the total unit cell volume. The crystal structure exhibits a hexagonal mesoporous channel with a width of 2.5 nm along the *c*-axis, accompanied by a smaller triangular channel (Fig. 2d). The angle of the mesoporous hexagonal cavity is 116.1° (Fig. 2c). The ligand **L1** adopts a non-planar configuration with C_{2v} symmetry. The two phenyl rings on the anthracene core extend toward the cavity centers, providing additional anchoring sites. The powder sample of Zr-705 was synthesized on a large scale under slightly modified conditions (SI-2). In SEM (Fig. S2) and TEM (Fig. S5) analyses, the samples retained a rod-like morphology with a smooth surface, exhibiting good crystallinity at the microscopic scale.

Dynamic light scattering (DLS) analysis indicated a uniform particle size distribution with an average diameter of approximately 2 μm (Fig. 3c). The diffraction peaks of the powder sample matched perfectly with those of the single crystal and the simulated pattern (Fig. 3a). This agreement demonstrated that the powder sample possessed the same structure as the single crystal, and also indicated high phase purity of the as-synthesized material. The NMR spectra of the degraded Zr-705 revealed a downfield shift of the ligand signal in Zr-705 as compared to the free one (Fig. S6). Infrared spectroscopy was used to confirm the structure of Zr-705. As shown in the spectrum (Fig. S7), the band at 1705 cm^{-1} is attributed to the carbonyl (C═O) stretching vibration of the ligand. Compared to the carbonyl vibration of the free ligand at 1696 cm^{-1}, the corresponding band in Zr-705 exhibited slight changes in both intensity and position, confirming the coordination of the carboxylate groups to the zirconium clusters. The bands observed at 1599 cm^{-1} and 1415 cm^{-1} were assigned to the asymmetric and symmetric stretching vibrations of the carboxylate groups, respectively,[63] further confirming the successful incorporation of the ligand in the Zr-705 framework. The bands at 1181 cm^{-1}, 1105 cm^{-1} and 1020 cm^{-1} were attributed to Zr–O bond vibrations. The band at 567 cm^{-1} was assigned to the asymmetric stretching vibration of the Zr–O–C linkage.[64] The porosity of Zr-705 was evaluated by nitrogen adsorption–desorption experiments at 77 K, which exhibited a BET surface area of 573.20 $m^2\ g^{-1}$ (Fig. 3d and Fig. S8), with pore sizes primarily distributed at 2.05 nm and 0.44 nm (Fig. 3e),[65] which were similar to the crystal structure. XPS analysis of Zr-705 revealed the presence of carbon, oxygen and zirconium elements on its surface (Fig. S17).

Thermogravimetric analysis (TGA) was employed to evaluate the thermal stability of Zr-705 (Fig. 3f), which demonstrated a high decomposition temperature (470 °C). The weight loss observed between 45 °C and 470 °C is primarily attributed to the loss of solvent (DEF). A sharp mass loss (38.6%) occurred in the range of 470–573 °C, corresponding to the thermal decomposition of the Zr-705 framework. The chemical stability of Zr-705 was assessed by immersing the sample in various solvents for one week. Zr-705 is insoluble but stable in common solvents as shown by the PXRD patterns which demonstrated that Zr-705 maintained a similar crystalline structure in these solvents (Fig. 3b). Furthermore, the framework remained stable when exposed to air. The acid and base stabilities of Zr-705 were monitored by FT-IR spectroscopy (Fig. S9). The spectra remained consistent across a wide pH range of 1 to 12; however, at higher

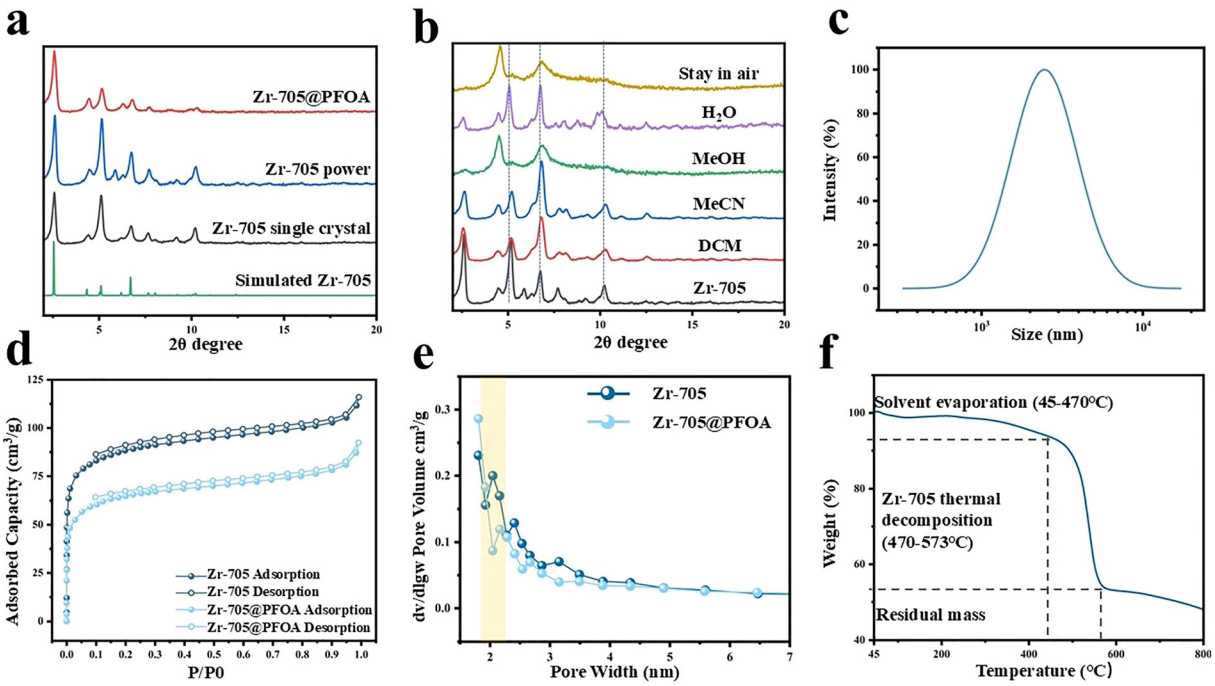

Fig. 3 (a) PXRD patterns of simulated, as-synthesized single crystal, as-synthesized powder, and Zr-705@PFOA samples. (b) PXRD patterns demonstrating the chemical stability of Zr-705 in various solvents. The minor shift may arise from the different solvents or air. (c) Dynamic light scattering (DLS) of a Zr-705 powder. (d) Nitrogen adsorption–desorption isotherms of Zr-705 and Zr-705@PFOA. (e) The pore size distribution profile of Zr-705 and Zr-705@PFOA. (f) Thermogravimetric analysis (TGA) curve of Zr-705.

pH values (13 or 14), distinct changes in the FT-IR spectra revealed the decomposition of the framework.

PFOA adsorption study

(1) PFOA adsorption performance. Zr-705 possessed a mesoporous network, open coordination sites, a conjugated hydrophobic cavity and high hydrothermal and chemical stability. We hypothesized that Zr-705 was suitable for PFOA adsorption. The activated Zr-705 was immersed in a PFOA solution (2000 ppm) and kept under static conditions at room temperature. The appearance of characteristic PFOA signals in the solid-state ^{19}F NMR spectrum confirmed the successful adsorption of PFOA from the aqueous solution by Zr-705 (Fig. 4a).

We further investigated the adsorption kinetics.[58,59,66] The adsorption process exhibited rapid kinetics, reaching equilibrium within 8 hours. The kinetic data were well-described by the pseudo-second-order model, with a correlation coefficient (R^2) of 0.99 and a rate of 2.25 mg mg^{-1} h^{-1} (Fig. 4b). Analysis of the kinetic data revealed that intraparticle diffusion was the rate-limiting step for mass transfer (Fig. S21). PFOA adsorption data were collected across a range of initial concentrations (350–4000 ppm). The experimental data were subsequently fitted using both the Freundlich (Fig. 4c) and Langmuir (Fig. 4d) models. The former model (R^2 = 0.97) exhibited a slightly higher correlation coefficient than the latter (R^2 = 0.96), indicating a better fit. This result suggested that the adsorption process likely occurred on a heterogeneous surface.[59] At an equilibrium concentration of 3995 ppm, Zr-705 achieved a remarkable adsorption capacity of 2031 mg g^{-1}. To the best of our knowledge, this value surpassed all previously reported materials, indicating that Zr-705 was the most effective MOF-adsorbent known to date (Fig. 4e). This high adsorption value was consistent with the result from mass balance analysis (Table S3).

During the measurement of the Zr-705 equilibrium adsorption isotherm, it was found that 1 mg of Zr-705 could efficiently remove PFOA from a 350 ppm solution (1 mL). Given that PFOA concentrations in real environments were typically below 300 ppm,[67–69] these results underscored the promising and broad application prospects of Zr-705 for practical water treatment. We further tested Zr-705 at a higher concentration of PFOA. Under static conditions (Fig. 5a), Zr-705 particles were immersed in a simulated wastewater solution containing 1000 ppm PFOA. After reaching equilibrium, the PFOA concentration in the supernatant was quantified (Fig. 5b). We constructed a packed column of Zr-705 particles to simulate dynamic flow conditions (Fig. 5c). After passing a 1000 ppm PFOA solution (3 mL) through the Zr-705 column (d = 8.5 mm, h = 8.0 mm, Zr-705 40 mg), PFOA was efficiently removed, yielding pure water (Fig. 5d).

To investigate the selectivity of Zr-705 in real environments, the adsorbent was immersed in a PFOA aqueous solution containing various interfering ions, including cations K^+, Na^+, Ca^{2+} and Mg^{2+}, and anions Cl^-, $Cr_2O_7^{2-}$, NO_3^-, SO_4^{2-} and CH_3COO^- (Fig. 6a). The results demonstrated that Zr-705 maintained stable PFOA adsorption performance, indicating

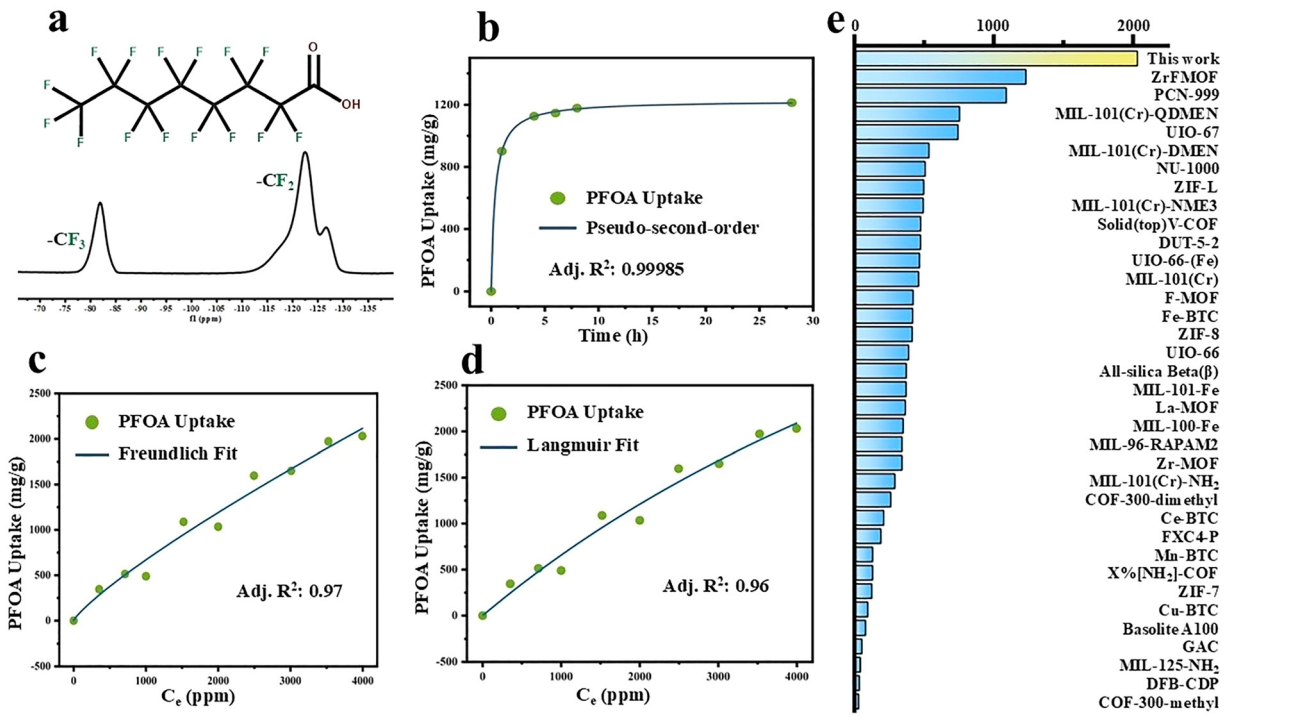

Fig. 4 (a) Solid-state ^{19}F NMR spectrum of Zr-705@PFOA. (b) Pseudo-second-order kinetic fitting for PFOA (2000 ppm, solid-to-liquid ratio 1 : 1) adsorption. Adsorption isotherms of PFOA (350 to 3995 ppm, solid-to-liquid ratio 1 : 1) on Zr-705 were fitted with the (c) Freundlich and (d) Langmuir models. (e) Comparison of the maximum PFOA adsorption capacity between Zr-705 and other reported materials (note: Adj.= adjusted).

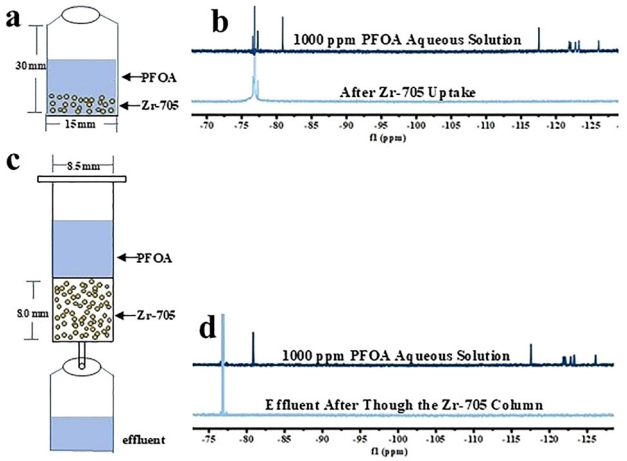

Fig. 5 (a) Schematic diagram of the experimental setup for static PFOA removal by Zr-705 (The bottle dimensions: d = 15.0 mm, h = 30.0 mm, and Zr-705 : 3 mg). (b) ^{19}F NMR spectra monitoring the removal of PFOA from solution by Zr-705 under static conditions. (c) Schematic diagram of the packed-column setup for dynamic PFOA removal by Zr-705. The column had an inner diameter of 8.5 mm, with a Zr-705 amount of 40 mg and a packing height of 8.0 mm. (d) ^{19}F NMR spectra monitoring the removal of PFOA from solution by Zr-705 under dynamic flow conditions.

that the co-existing ions had negligible impact on its adsorption capability. Furthermore, Zr-705 could be easily regenerated from Zr-705@PFOA by methanol treatment. After methanol washing, degradative ^{19}F NMR analysis of the regenerated material showed no detectable PFOA signals, confirming the effective removal (Fig. 6b). Then, the regenerated Zr-705 could be reused for the next cycle (Fig. 6c). It was noteworthy that Zr-705 was stable in acidic environments, and it was unstable only in high pH solutions (pH 13 and pH 14, Fig. S9). Normally, the PFOA solution is acidic (the pH values for 1–4 mg mL^{-1} PFOA in water are 6.0, 5.0, 4.0 and 3.0 respectively). Furthermore, when 1–4 mg Zr-705 were added to the above solutions, respectively, the pH kept the same values. Zr-705 was a neutral material and a small amount only changed the volume slightly and the pH values of the solutions.

The PXRD patterns collected before and after PFOA adsorption are similar, confirming that the structural integrity of the Zr-705 framework is maintained throughout the adsorption process (Fig. 3a).

(2) PFOA adsorption mechanism. In order to probe the detailed interactions, we tried several times to grow a single crystal of the complex Zr-705@PFOA; however, we could not get it. As a result, the crystal structure of Zr-705@PFOA was not obtained. Then, we examined the BET area, pore sizes after adsorption, changes in FT-IR and NMR spectra, electrostatic potentials and molecular simulation to analyse the PFOA adsorption mechanism.

Comparison of the N_2 adsorption curves of Zr-705 and Zr-705@PFOA revealed that after PFOA loading, the BET specific surface area decreased from 573.20 m^2 g^{-1} to 114.89 m^2 g^{-1} (Fig. 3d). The disappearance of the mesoporous peak of Zr-705@PFOA indicates that the mesoporous cavity was blocked by PFOA molecules (Fig. 3e).

To clarify the surface composition, XPS analysis was conducted. Before adsorption, the Zr-705 sample contained only carbon, oxygen, and zirconium (Fig. S17). However, after adsorption, fluorine appeared in the sample, indicating the binding of a substantial amount of PFOA. The C 1s spectra before and after adsorption were shown in Fig. S18 and S19, respectively. Before adsorption, the spectrum contained two peaks, *i.e.* C–C (284.80 eV) and O–C=O (288.67 eV) (Fig. S18). After adsorption, two new peaks appeared, *i.e.* CF_2 (291.73 eV) and CF_3 (294.00 eV) (Fig. S19), further confirming the binding between Zr-705 and PFOA.[70]

We compared the FT-IR spectra of pristine Zr-705 and Zr-705@PFOA (Fig. 7a). FT-IR data showed that the stretching vibration peaks of PFOA at 1233, 1205, and 1148 cm^{-1} shifted to 1240, 1209, and 1145 cm^{-1}, respectively, in the Zr-705@PFOA

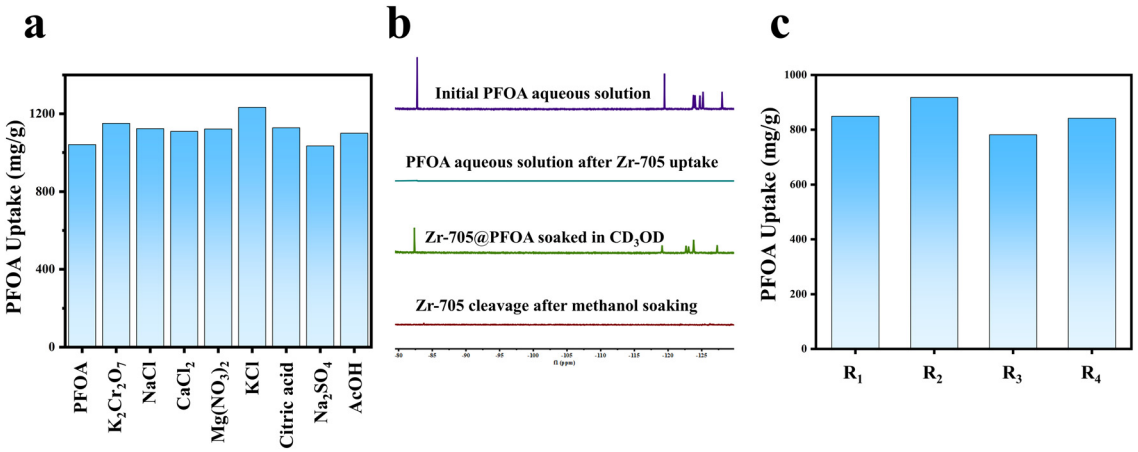

Fig. 6 (a) PFOA adsorption capacity of Zr-705 in the presence of various interfering ions. The concentration of PFOA was 3 mg mL^{-1} (pH 5.0), the concentration of interfering ions was 3 mg mL^{-1}, and the solid-to-liquid ratio was 2 : 1. (b) ^{19}F NMR monitoring of the Zr-705 regeneration process using methanol. (c) Recyclability of Zr-705 over four consecutive adsorption–desorption cycles. The concentration of PFOA was 4 mg mL^{-1}, and the solid-to-liquid ratio was 3 : 1.

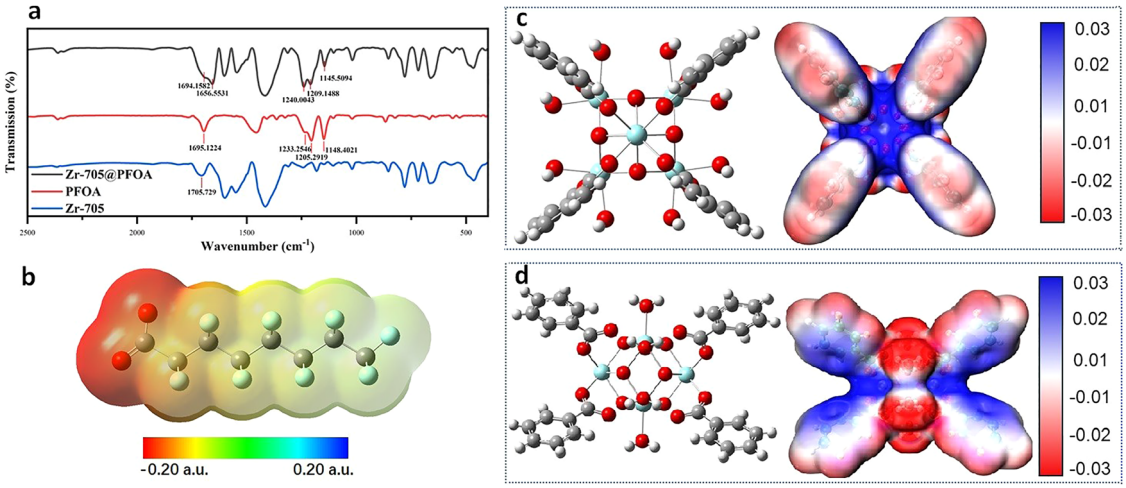

Fig. 7 (a) FT-IR spectrum of Zr-705@PFOA. (b) Electrostatic potential (ESP) distribution map of a PFOA anion. (c) ESP (a.u.) of a zirconium cluster (top view). (d) ESP (a.u.) of a zirconium cluster (front view).

composite. In PFOA, 1148 cm^{-1} is assigned to the symmetric stretching vibration of $-CF_2$, 1205 cm^{-1} is the asymmetric stretching vibration of $-CF_3$, and 1233 cm^{-1} is the asymmetric stretching vibration of $-CF_2$.[71] These characteristic signals demonstrate that PFOA was successfully adsorbed and the changes indicate interactions with the framework. Meanwhile, a distinct shift was observed in the characteristic peak corresponding to the C═O stretching vibration within the range of 1650–1700 cm^{-1}. This change indicates a strong interaction between the carboxylate group of PFOA and Zr-705.[58]

Comparison of the solid-state NMR data showed that the characteristic peak of the ^{19}F signal at δ −82.5 ppm (CF_3) shifted to δ −81.8 ppm in Zr-705@PFOA. (Fig. 4a) The four peaks around −122.0 ppm in free PFOA were merged into a single broad peak at δ −112.4 ppm in Zr-705@PFOA (Fig. S14 and S15).[72] This observation confirmed the binding of PFOA to the framework and also indicated strong interactions between the hydrophobic chain of PFOA and Zr-705. The ^{19}F signal suggested that the PFOA molecule might adopt an all-trans conformation, which was similar to the reported Zr-MOF.[56]

Electrostatic potentials (ESP) of Zr-705 and PFOA were calculated by Gaussian[73,74] and Multiwfn,[75] and the results were visualized using VMD.[76] Within the PFOA anion, the negative charge was concentrated on the carboxylate group (Fig. 7b). Strong positive potential (Fig. 7c and d) distributed around the zirconium cluster. These regions are electron-deficient and are susceptible to nucleophilic attack. The ESP calculation clearly indicated strong electrostatic interactions between PFOA and Zr-705.

Finally, we performed molecular simulation to mimic the binding of PFOA to Zr-705. Based on PLATON calculation, the Zr-705 framework has a solvent-accessible volume of 22 653.2 $Å^3$. Rebek *et al.* introduced the concept of "packing coefficients" (PCs), and a PC value of 0.55 ± 0.1 was suggested as the optimum for host–guest complexes.[77] We used Multiwfn software to calculate the volume of PFOA and found that the volume was 530 $Å^3$. Thus, the theoretical maximum loading of PFOA is 24. The simulated adsorption mode of PFOA in Zr-705 is shown in Fig. S28, and the simulated interactions between PFOA and Zr-705 are shown in Table S4. From the simulation, we could infer that the guests 1–6 (big central cavity) bound to Zr-705 through electrostatic interactions with O–Zr distances in the range of 5.3–6.5 Å, guests 7–12 (small cavity) bound to Zr-705 through C–H···F interactions with C···F distances in the range of 2.5–3.9 Å; and guests 13–24 (periphery) bound to Zr-705 through O–H···F hydrogen bonds with O···F distances in the range of 2.6–3.4 Å. Based on the simulation, the schematic illustration of PFOA adsorption by Zr-705 was proposed (Fig. S29).

Conclusions

In this work, we report the synthesis of a novel zirconium-based metal–organic framework, designated as Zr-705. The ligand in Zr-705 features an anthracene core, with phenyl rings on both sides extending into the pore channels. This structural configuration not only increases the internal surface area of the MOF but also provides conjugated systems, providing anchoring sites for guest molecules. Zr-705 adopts a csq topology and possesses one-dimensional mesoporous channels (2.5 nm pore aperture) along the *c*-axis. Additionally, the zirconium clusters offer multiple open coordination sites and exhibit high chemical and physical stability. Zr-705 exhibited exceptional PFOA adsorption performance, achieving a record adsorption capacity of 2031 mg g^{-1}. Concurrently, it demonstrated rapid adsorption kinetics with a rate constant of 2.25 mg mg^{-1} h^{-1}, which is well-described by the pseudo-second-order kinetic model. In practical application scenarios, Zr-705 achieved efficient removal of PFOA from aqueous solutions even under dynamic flow conditions. It also demonstrated high selectivity, and excellent reusability. Besides the adsorption performance, the mechanism was examined based on the BET area, pore sizes after adsorption, changes in FT-IR and solid-state NMR spectra, electrostatic potentials and molecular simulation.

Author contributions

Xiaoyun Su performed Zr-705 synthesis, the PFOA adsorption study and wrote the draft. Bo Yuan studied the stability of Zr-705. Peng Luo was responsible for the molecular simulation. Wei Xu performed the X-ray experiment, Wen-Cai Ye and Ren-Wang Jiang (ORCID: 0000-0002-0730-9866) designed the experiments and revised the manuscript.

Conflicts of interest

There are no conflicts to declare.

Data availability

All other relevant data generated and analysed during this study, which include experimental, spectroscopic and crystallographic, are included in the supplementary information (SI). Source data are provided with this paper. Supplementary information is available. See DOI: https://doi.org/10.1039/d6ma00291a.

CCDC 2532991 contains the supplementary crystallographic data for this paper.[78]

Acknowledgements

This work was supported by the Science and Technology Project in Guangzhou (grant number 202102070001), and the Natural Science Foundation of Guangdong province (2024A1515011191). Special thanks are given to the public research platform of the College of Pharmacy, Jinan University and Ms Jiang Qinqin, Drug Screening Platform, Public Technology Service Center of Guangzhou Laboratory.

References

1 S. C. E. Leung, P. Shukla, D. Chen, E. Eftekhari, H. An, F. Zare, N. Ghasemi, D. Zhang, N.-T. Nguyen and Q. Li, Emerging technologies for PFOS/PFOA degradation and removal: A review, *Sci. Total Environ.*, 2022, **827**, 153669.

2 S. E. Fenton, A. Ducatman, A. Boobis, J. C. DeWitt, C. Lau, C. Ng, J. S. Smith and S. M. Roberts, Per- and polyfluoroalkyl substance toxicity and human health review: Current state of knowledge and strategies for informing future research, *Environ. Toxicol. Chem.*, 2021, **40**, 606–630.

3 J. Glüge, M. Scheringer, I. T. Cousins, J. C. DeWitt, G. Goldenman, D. Herzke, R. Lohmann, C. A. Ng, X. Trier and Z. Wang, An overview of the uses of per- and polyfluoroalkyl substances (PFAS), *Environ. Sci.: Processes Impacts*, 2020, **22**, 2345–2373.

4 M. Antonopoulou, A. Spyrou, A. Tzamaria, I. Efthimiou and V. Triantafyllidis, Current state of knowledge of environmental occurrence, toxic effects, and advanced treatment of PFOS and PFOA, *Sci. Total Environ.*, 2024, **913**, 169332.

5 M. L. Brusseau, R. H. Anderson and B. Guo, PFAS concentrations in soils: Background levels versus contaminated sites, *Sci. Total Environ.*, 2020, **740**, 140017.

6 A. Podder, A. H. M. A. Sadmani, D. Reinhart, N. B. Chang and R. Goel, Per and poly-fluoroalkyl substances (PFAS) as a contaminant of emerging concern in surface water: A transboundary review of their occurrences and toxicity effects, *J. Hazard. Mater.*, 2021, **419**, 126361.

7 D. Brooke, A. Footitt and T. Nwaogu, *Environmental Risk Evaluation Report: Perflurooctanesulphonate (PFOS)*, Environment Agency, UK, 2004.

8 X. Lim, Could the world go PFAS-free? Proposal to ban 'forever chemicals' fuels debate, *Nature*, 2023, **620**, 24–27.

9 *Ministry of Ecology and Environment of the People's Republic of China. List of Key Controlled New Pollutants (2023 Edition)*. 2023.

10 W. A. Gebbink and S. P. J. van Leeuwen, Environmental contamination and human exposure to PFASs near a fluorochemical production plant: Review of historic and current PFOA and GenX contamination in the Netherlands, *Environ. Int.*, 2020, **137**, 105583.

11 R. Cariou, B. Veyrand, A. Yamada, A. Berrebi, D. Zalko, S. Durand, C. Pollono, P. Marchand, J. C. Leblanc, J. P. Antignac and B. Le Bizec, Perfluoroalkyl acid (PFAA) levels and profiles in breast milk, maternal and cord serum of French women and their newborns, *Environ. Int.*, 2015, **84**, 71–81.

12 F. Sella, C. Licini, M. Lombó, C. Giommi, D. Carbonari, M. Mattioli Belmonte and O. Carnevali, Unveiling the toxic effects of perfluorooctanoic acid on osteoblast function and extracellular matrix deposition using 2D and 3D models, *Cell Death Discov.*, 2026, **12**, 10.

13 H. L. Shane, R. Baur, E. Lukomska, L. Weatherly and S. E. Anderson, Immunotoxicity and allergenic potential induced by topical application of perfluorooctanoic acid (PFOA) in a murine model, *Food Chem. Toxicol.*, 2020, **136**, 111114.

14 K. Steenland, S. Kugathasan and D. B. Barr, PFOA and ulcerative colitis, *Environ. Res.*, 2018, **165**, 317–321.

15 R. N. Guan, F. Luan, N. Q. Li, Z. Q. Qiu, W. C. Liu, Z. Y. Cui, C. Y. Zhao and X. Li, Identification of molecular initiating events and key events leading to endocrine disrupting effects of PFOA: Integrated molecular dynamic, transcriptomic, and proteomic analyses, *Chemosphere*, 2022, **307**, 135881.

16 V. Berg, T. H. Nøst, S. Hansen, A. Elverland, A. S. Veyhe, R. Jorde, J. Ø. Odland and T. M. Sandanger, Assessing the relationship between perfluoroalkyl substances, thyroid hormones and binding proteins in pregnant women; a longitudinal mixed effects approach, *Environ. Int.*, 2015, **77**, 63–69.

17 J. J. Shearer, C. L. Callahan, A. M. Calafat, W. Y. Huang, R. R. Jones, V. S. Sabbisetti, N. D. Freedman, J. N. Sampson, D. T. Silverman, M. P. Purdue and J. N. Hofmann, Serum concentrations of per- and polyfluoroalkyl substances and risk of renal cell carcinoma, *J. Natl. Cancer Inst.*, 2021, **113**, 580–587.

18 J. W. Stanifer, H. M. Stapleton, T. Souma, A. Wittmer, X. L. Zhao and L. E. Boulware, Perfluorinated chemicals as

emerging environmental threats to kidney health: A scoping review, *Clin. J. Am. Soc. Nephrol.*, 2018, **13**, 1479–1492.

19 I. Šabović, I. Cosci, L. De Toni, A. Ferramosca, M. Stornaiuolo, A. Di Nisio, S. Dall'Acqua, A. Garolla and C. Foresta, Perfluoro-octanoic acid impairs sperm motility through the alteration of plasma membrane, *J. Endocrinol. Invest.*, 2020, **43**, 641–652.

20 G. Nielsen, E. Reed, B. Lara, D. H. Sherr, W. J. Heiger Bernays, T. Hyötyläinen, T. F. Webster and J. J. Schlezinger, Integrated assessment of the effects of PFOA exposure on hepatic transcriptome and lipid profiles in mice expressing human PPARα, *Toxicol. Appl. Pharmacol.*, 2026, **506**, 117658.

21 J. Choi, J. Y. Kim and H. J. Lee, Human evidence of perfluorooctanoic acid (PFOA) exposure on hepatic disease: A systematic review and meta-analysis, *Int. J. Environ. Res. Public Health*, 2022, **19**, 11318.

22 W. X. Cheng and C. A. Ng, A permeability-limited physiologically based pharmacokinetic (PBPK) model for perfluorooctanoic acid (PFOA) in male rats, *Environ. Sci. Technol.*, 2017, **51**, 9930–9939.

23 A. Blais, A. Loan, E. Cho, A. Woodtke, H. Moteshareie, L. M. Bradford, G. Zhang, G. Pelletier, M. Navarro, M. J. Meier, A. Nong, R. Aranda Rodriguez, K. M. Eccles, D. Prescott and A. F. Tayabali, PFOS and PFOA exposure induces liver injury and sex-dependent immune effects in C57BL/6 mice, *iScience*, 2026, **29**, 114693.

24 Y. T. Du, C. J. Chen, G. D. Zhou, Z. Z. Cai, Q. H. Man, B. L. Liu and W. C. Wang, Perfluorooctanoic acid disrupts thyroid-specific genes expression and regulation via the TSH-TSHR signaling pathway in thyroid cells, *Environ. Res.*, 2023, **239**, 117372.

25 A. F. Treschow, E. Martiny, C. T. Gutierrez, A. A. Niklas, M. Scholze, A. M. Vinggaard and M. J. Valente, Embryotoxicity and mixture effects of legacy PFAS in a human iPSC-based 3D model, *Cell Biol. Toxicol.*, 2026, **42**, 24.

26 M. Z. Li, C. K. Xu, L. W. Li, F. M. Gao, C. Xu, Y. F. Yu, C. Huang, Y. N. Liu, X. M. Shen and J. Y. Hu, Placentation disruption by perfluorooctanoic acid and perfluorooctanesulfonate in human trophoblast organoids, *Environ. Sci. Technol.*, 2025, **59**, 20263–20275.

27 S. P. Chetverikov and O. N. Loginov, A new Ensifer adhaerens strain M1 is capable of transformation of perfluorocarboxylic acids, *Microbiology*, 2019, **88**, 115–117.

28 V. P. Beškoski, A. Yamamoto, T. Nakano, K. Yamamoto, C. Matsumura, M. Motegi, L. S. Beškoski and H. Inui, Defluorination of perfluoroalkyl acids is followed by production of monofluorinated fatty acids, *Sci. Total Environ.*, 2018, **636**, 355–359.

29 Q. Luo, S. T. Liang and Q. G. Huang, Laccase induced degradation of perfluorooctanoic acid in a soil slurry, *J. Hazard. Mater.*, 2018, **359**, 241–247.

30 D. R. Ryan, C. K. Baldus, S. M. Kteeba, M. Samuel, Q. Q. Dong, Y. Wang, L. D. Guo, B. K. Mayer and P. McNamara, Peroxi-electrocoagulation for PFAS mitigation: The impact of water quality and dissolved organic matter on removal pathways, *ACS EST Eng.*, 2025, **5**, 1202–1214.

31 T. H. Mu and K. Y. Kim, Emerging investigator series: Impacts of aeration flow rates and bubble sizes on PFOA/PFOS removal in electrocoagulation, *Environ. Sci.: Water Res. Technol.*, 2023, **9**, 1783–1791.

32 D. J. Burns, P. Stevenson and P. J. C. Murphy, PFAS removal from groundwaters using surface-active foam fractionation, *Remediation J.*, 2021, **31**, 19–33.

33 P. McCleaf, Y. Kjellgren and L. Ahrens, Foam fractionation removal of multiple per- and polyfluoroalkyl substances from landfill leachate, *AWWA Water Sci.*, 2021, **3**, e1238.

34 Y. C. Lee, M. J. Chen, C. P. Huang, J. Kuo and S. L. Lo, Efficient sonochemical degradation of perfluorooctanoic acid using periodate, *Ultrason. Sonochem.*, 2016, **31**, 499–505.

35 T. Sidnell, A. J. C. Cobos, J. Hurst, J. Lee and M. J. Bussemaker, Flow and temporal effects on the sonolytic defluorination of perfluorooctane sulfonic acid, *Ultrason. Sonochem.*, 2023, **101**, 106667.

36 N. Y. Yang, S. S. Yang, Q. Q. Ma, C. Beltran, Y. Q. Guan, M. Morsey, E. Brown, S. Fernando, T. M. Holsen, W. Zhang and Y. Yang, Solvent-free nonthermal destruction of PFAS chemicals and PFAS in sediment by piezoelectric ball milling, *Environ. Sci. Technol. Lett.*, 2023, **10**, 198–203.

37 N. Wang, H. Q. Lv, Y. Q. Zhou, L. H. Zhu, Y. Hu, T. Majima and H. Q. Tang, Complete defluorination and mineralization of perfluorooctanoic acid by a mechanochemical method using alumina and persulfate, *Environ. Sci. Technol.*, 2019, **53**, 8302–8313.

38 A. L. Garcia Costa, A. Savall, J. A. Zazo, J. A. Casas and K. Groenen Serrano, On the role of the cathode for the electro-oxidation of perfluorooctanoic acid, *Catalysts*, 2020, **10**, 902.

39 S. Annamalai, N. Kim and S. Hwang, Enhanced PFOA degradation via persulfate-assisted electrochemical oxidation: Performance, mechanistic insights, and toxicity analysis, *J. Environ. Chem. Eng.*, 2025, **13**, 119424.

40 M. Trojanowicz, I. Bartosiewicz, A. Bojanowska Czajka, T. Szreder, K. Bobrowski, G. Nałęcz Jawecki, S. Męczyńska Wielgosz and H. Nichipor, Application of ionizing radiation in decomposition of perfluorooctane sulfonate (PFOS) in aqueous solutions, *Chem. Eng. J.*, 2020, **379**, 122303.

41 S. A. O. Olson, N. S. Borker, G. D. Frost, H. Hatakka, I. Kornev, S. McNamara, H. L. Ring, D. Buckley, Z. N. Liu, P. Kupias, S. Manninen, P. Ajo and K. I. Hunter, PFAS remediation by commercially available pulsed plasma technology, *ACS EST Water*, 2025, **5**, 4375–4386.

42 V. Jovicic, M. J. Khan, A. Zbogar Rasic, N. Fedorova, A. Poser, P. Swoboda and A. Delgado, Degradation of low concentrated perfluorinated compounds (PFCs) from water samples using non-thermal atmospheric plasma (NTAP), *Energies*, 2018, **11**, 1290.

43 K. Pavithra, B. M. Sharma and P. Chakraborty, An overview of the occurrence and remediation of perfluorooctanoic acid (PFOA) in wastewater-recommendations for cost-effective removal techniques in developing economies, *Curr. Opin. Environ. Sci. Health*, 2024, **41**, 100565.

44 Y. H. Wen, Á. Rentería Gómez, G. S. Day, M. F. Smith, T. H. Yan, R. O. K. Ozdemir, O. Gutierrez, V. K. Sharma, X. M. Ma and H. C. Zhou, Integrated photocatalytic reduction and oxidation of perfluorooctanoic acid by metal-organic frameworks: Key insights into the degradation mechanisms, *J. Am. Chem. Soc.*, 2022, **144**, 11840–11850.

45 Y. H. Wen, A. Kirchon, G. S. Day, H. Y. Lin, M. F. Smith, A. Boehme, R. O. K. Ozdemir, V. K. Sharma, X. M. Ma and H. C. Zhou, Photocatalytic degradation of perfluorooctanoic acid (PFOA) by metal organic framework MIL-177-HT: New insights into the role of specific surface area, charge separation and dimensionality, *Sep. Purif. Technol.*, 2025, **354**, 128877.

46 R. R. Liang, Y. B. Fu, Z. S. Han, Y. H. Yang, V. I. Bakhmutov, Z. Y. Liu, J. Rushlow and H. C. Zhou, A robust pyrazolate metal-organic framework for integrated perfluorooctanoic acid concentration and degradation, *Nat. Water*, 2024, **2**, 1218–1225.

47 P. H. Fang, L. L. Qu, Z. S. Ma, C. Q. Han, Z. D. Li, L. Wang, K. Zhou, J. B. Li and X. Y. Liu, Full-color emissive zirconium-organic frameworks constructed via in situ "one-pot" single-site modification for tryptophan detection and energy transfer, *Angew. Chem., Int. Ed.*, 2025, **64**, e202414026.

48 X. J. Hu, Y. J. Zhang, H. Z. Liu, M. H. Zhan, J. Chen, Z. M. Liu and H. X. Chen, Simultaneous detection and decontamination of dichromate ions: The fluorescence response and photocatalysis of thiadiazole-modified Zr-metal-organic frameworks, *J. Agric. Food Chem.*, 2023, **71**, 20575–20584.

49 J. D. Pang, Z. Y. Di, J. S. Qin, S. Yuan, C. T. Lollar, J. L. Li, P. Zhang, M. Y. Wu, D. Q. Yuan, M. C. Hong and H. C. Zhou, Precisely embedding active sites into a mesoporous Zr-framework through linker installation for high-efficiency photocatalysis, *J. Am. Chem. Soc.*, 2020, **142**, 15020–15026.

50 C. Fiankor, J. Nyakuchena, R. S. H. Khoo, X. Zhang, Y. C. Hu, S. Z. Yang, J. Huang and J. Zhang, Symmetry-guided synthesis of N,N′-bicarbazole and porphyrin-based mixed-ligand metal-organic frameworks: Light harvesting and energy transfer, *J. Am. Chem. Soc.*, 2021, **143**, 20411–20418.

51 I. Abánades Lázaro, C. J. R. Wells and R. S. Forgan, Multivariate modulation of the Zr MOF UiO-66 for defect-controlled combination anticancer drug delivery, *Angew. Chem., Int. Ed.*, 2020, **132**, 5249–5255.

52 H. D. Cornell, A. T. Sose, S. Ilic, S. Chinnabattigalla, N. E. Lidman, C. M. Oldmixon, X. Z. Yang, S. A. Deshmukh and A. J. Morris, Photoactivated multivariate metal-organic frameworks for on-demand drug release: The role of host-guest interactions, *J. Am. Chem. Soc.*, 2025, **147**, 7423–7432.

53 Y. J. Chen, P. Li, J. A. Modica, R. J. Drout and O. K. Farha, Acid-resistant mesoporous metal-organic framework toward oral insulin delivery: Protein encapsulation, protection, and release, *J. Am. Chem. Soc.*, 2018, **140**, 5678–5681.

54 Y. J. Chen, F. Jiménez Ángeles, B. F. Qiao, M. D. Krzyaniak, F. R. Sha, S. Kato, X. Y. Gong, C. T. Buru, Z. J. Chen, X. Zhang, N. C. Gianneschi, M. R. Wasielewski, M. Olvera de la Cruz and O. K. Farha, Insights into the enhanced catalytic activity of cytochrome *c* when encapsulated in a metal-organic framework, *J. Am. Chem. Soc.*, 2020, **142**, 18576–18582.

55 P. Li, Q. S. Chen, T. C. Wang, N. A. Vermeulen, B. L. Mehdi, A. Dohnalkova, N. D. Browning, D. K. Shen, R. Anderson, D. A. Gómez Gualdrón, F. M. Cetin, J. Jagiello, A. M. Asiri, J. F. Stoddart and O. K. Farha, Hierarchically engineered mesoporous metal-organic frameworks toward cell-free immobilized enzyme systems, *Chem*, 2018, **4**, 1022–1034.

56 W. P. Huang, J. C. Liu, F. Wang, W. Xu, Z. M. Tao, D. A. Middleton, C. D. Liu, S. Q. Qin, W. C. Ye and R. W. Jiang, Encapsulation of toxic liquid molecules and adsorption of water pollutants by a versatile pre-organized single crystalline coating material, *Inorg. Chem. Front.*, 2025, **12**, 3531–3544.

57 R. Li, S. Alomari, R. Stanton, M. C. Wasson, T. Islamoglu, O. K. Farha, T. M. Holsen, S. M. Thagard, D. J. Trivedi and M. Wriedt, Efficient removal of per- and polyfluoroalkyl substances from water with zirconium-based metal-organic frameworks, *Chem. Mater.*, 2021, **33**, 3276–3285.

58 R. R. Liang, S. Q. Xu, Z. S. Han, Y. H. Yang, K. Y. Wang, Z. H. Huang, J. Rushlow, P. Y. Cai, P. Samorì and H. C. Zhou, Exceptionally high perfluorooctanoic acid uptake in water by a zirconium-based metal-organic framework through synergistic chemical and physical adsorption, *J. Am. Chem. Soc.*, 2024, **146**, 9811–9818.

59 K. Sini, D. Bourgeois, M. Idouhar, M. Carboni and D. Meyer, Metal-organic framework sorbents for the removal of perfluorinated compounds in an aqueous environment, *New J. Chem.*, 2018, **42**, 17889–17894.

60 R. R. Liang, Y. H. Yang, Z. S. Han, V. I. Bakhmutov, J. Rushlow, Y. B. Fu, K. Y. Wang and H. C. Zhou, Zirconium-based metal-organic frameworks with free hydroxy groups for enhanced perfluorooctanoic acid uptake in water, *Adv. Mater.*, 2024, **36**, 2407194.

61 A. L. Spek, Single-crystal structure validation with the program PLATON, *J. Appl. Crystallogr.*, 2003, **36**, 7–13.

62 A. L. Spek, Structure validation in chemical crystallography, *Acta Crystallogr. D*, 2009, **65**, 148–155.

63 J. H. Cavka, S. Jakobsen, U. Olsbye, N. Guillou, C. Lamberti, S. Bordiga and K. P. Lillerud, A new zirconium inorganic building brick forming metal organic frameworks with exceptional stability, *J. Am. Chem. Soc.*, 2008, **130**, 13850–13851.

64 T. L. Ma, D. J. Liu, Z. Liu, J. F. Xu, Y. Dong, G. L. Chen and Z. Yun, 12-Tungstophosphoric acid-encapsulated metal-organic framework UiO-66: A promising catalyst for the esterification of acetic acid with n-butanol, *J. Taiwan Inst. Chem. Eng.*, 2022, **133**, 104277.

65 A. Schaate, S. Dühnen, G. Platz, S. Lilienthal, A. M. Schneider and P. Behrens, A novel Zr-based porous coordination polymer containing azobenzenedicarboxylate as a linker, *Eur. J. Inorg. Chem.*, 2012, 790–796.

66 S. Wang, J. Cui, B. Liang, Y. Liu, J. He, J. Cui and C. Shan, Efficient adsorption of methyl orange by MgMn-LDHs under the synergistic action of multi-mechanism models, *Appl. Surf. Sci.*, 2026, **735**, 166662.

67 V. A. Arias E, M. Mallavarapu and R. Naidu, Identification of the source of PFOS and PFOA contamination at a military air base site, *Environ. Monit. Assess.*, 2015, **187**, 4111.
68 X. F. Hang, X. R. Chen, J. Q. Luo, W. F. Cao and Y. H. Wan, Removal and recovery of perfluorooctanoate from wastewater by nanofiltration, *Sep. Purif. Technol.*, 2015, **145**, 120–129.
69 Z. Y. Liu, Y. L. Lu, P. Wang, T. Y. Wang, S. J. Liu, A. C. Johnson, A. J. Sweetman and Y. Baninla, Pollution pathways and release estimation of perfluorooctane sulfonate (PFOS) and perfluorooctanoic acid (PFOA) in central and eastern China, *Sci. Total Environ.*, 2017, **580**, 1247–1256.
70 C. Q. Chen, D. Z. Chen, S. S. Xie, H. Y. Quan, X. B. Luo and L. Guo, Adsorption Behaviors of Organic Micropollutants on Zirconium Metal–Organic Framework UiO-66: Analysis of Surface Interactions, *ACS Appl. Mater. Interfaces*, 2017, **9**(46), 41043–41054.
71 R. Dalapati, J. F. Shi, M. Hunter and L. Zang, Dual-functional metal–organic framework for efficient removal and fluorescent detection of perfluorooctanoic acid (PFOA) from water, *J. Mater. Chem. C*, 2025, **13**, 16753–16762.
72 H. Q. Lv, N. Wang, L. H. Zhu, Y. Q. Zhou, W. J. Li and H. Q. Tang, Alumina-mediated mechanochemical method for simultaneously degrading perfluorooctanoic acid and synthesizing a polyfluoroalkene, *Green Chem.*, 2018, **20**, 2526–2533.
73 M. J. Frisch, G. W. Trucks, H. B. Schlegel, G. E. Scuseria, M. A. Robb, J. R. Cheeseman, G. Scalmani, V. Barone, G. A. Petersson, H. Nakatsuji, X. Li, M. Caricato, A. V. Marenich, J. Bloino, B. G. Janesko, R. Gomperts, B. Mennucci, H. P. Hratchian, J. V. Ortiz, A. F. Izmaylov, J. L. Sonnenberg, D. Williams-Young, F. Ding, F. Lipparini, F. Egidi, J. Goings, B. Peng, A. Petrone, T. Henderson, D. Ranasinghe, V. G. Zakrzewski, J. Gao, N. Rega, G. Zheng, W. Liang, M. Hada, M. Ehara, K. Toyota, R. Fukuda, J. Hasegawa, M. Ishida, T. Nakajima, Y. Honda, O. Kitao, H. Nakai, T. Vreven, K. Throssell, J. A. Montgomery Jr., J. E. Peralta, F. Ogliaro, M. J. Bearpark, J. J. Heyd, E. N. Brothers, K. N. Kudin, V. N. Staroverov, T. A. Keith, R. Kobayashi, J. Normand, K. Raghavachari, A. P. Rendell, J. C. Burant, S. S. Iyengar, J. Tomasi, M. Cossi, J. M. Millam, M. Klene, C. Adamo, R. Cammi, J. W. Ochterski, R. L. Martin, K. Morokuma, O. Farkas, J. B. Foresman and D. J. Fox, *Gaussian 16, Revision C.01*, Gaussian, Inc., Wallingford, CT, 2016.
74 R. Dennington, T. A. Keith and J. M. Millam, *GaussView, Version 6.1*, Semichem Inc., Shawnee Mission, KS, 2016.
75 T. Lu, A comprehensive electron wavefunction analysis toolbox for chemists, Multiwfn, *J. Chem. Phys.*, 2024, **161**, 082503.
76 W. Humphrey, A. Dalke and K. Schulten, VMD: Visual molecular dynamics, *J. Mol. Graph.*, 1996, **14**, 33–38.
77 S. Mecozzi and J. Rebek Jr., The 55% Solution: A Formula for Molecular Recognition in the Liquid State, *Chem. – Eur. J.*, 1998, **4**, 1016–1022.
78 CCDC 2532991: Experimental Crystal Structure Determination, 2026, DOI: 10.5517/ccdc.csd.cc2r0sdz.